

# Microstructure, tensile properties and fracture behaviour of an Al-Cu-Li-Mg-Zr alloy 8090

T. S. SRIVATSAN

*Department of Mechanical Engineering, The University of Akron, Akron, Ohio 44325, USA*

T. ALAN PLACE\*

*Department of Mechanical Engineering, University of Idaho, Moscow, Idaho 83843, USA*

The addition of lithium to aluminium alloys has the potential for providing a class of high strength alloys with exceptional properties suitable for aerospace applications. One such candidate is 8090, a precipitation hardenable Al-Li-Cu-Mg alloy. Detailed optical microscopical observations were used to analyse the intrinsic microstructural features of the alloy. It is shown that microstructural characteristics have a pronounced influence on tensile properties and fracture behaviour of the alloy in the peak-aged, maximum strength condition. Tensile test results indicate that the alloy has property combinations comparable with other high strength commercial aluminium alloys. The elongation and reduction in area are higher in the transverse direction of the extruded plate. A change in fracture mode was observed with direction of testing. We rationalize such behaviour based on the grain structure of the material, and the nature, distribution and morphology of the second-phase particles. An attempt is made to discuss the kinetics of the fracture process in terms of several competing mechanistic effects involving intrinsic microstructural features, deformation characteristics of the matrix, brittleness of the grain boundary precipitates and grain boundary failure. The role of stress on particle fracture is highlighted.

## 1. Introduction

The critical need to improve the efficiency and performance of aircraft, coupled with continuing emphasis on minimum weight, has prompted interest in the use of lighter-weight and stiffer materials. Lithium-containing aluminium alloys are attractive alternatives to existing high strength aluminium alloys and carbon-fibre composites for stiffness-critical airframe structures. The family of aluminium-lithium alloys offers the unique promise of weight savings and desirable combinations of high monotonic tensile and yield strengths, decreased densities, increased stiffness, improved thermal stability and good resistance to the propagation of fatigue cracks have emerged as the most attractive material for critical airframe components. These alloys have engendered an unprecedented widespread interest in the aerospace industry on account of their potential to replace the conventional aluminium alloys. In recent years, lithium-containing aluminium alloys have been the subject of increased research activity aimed at understanding their various metallurgical and mechanical characteristics [1-5].

In the maximum strength, peak-aged (PA) condition, ductility and fracture toughness of lithium-containing aluminium alloys is unacceptably low for many potential applications on account of their susceptibility to grain boundary fracture. This problem is rationalized in terms of several concurrent and mutually competitive factors involving the following

(i) Presence of coarse grain boundary precipitates, often a more stable phase than the matrix strengthening phase [6-13].

(ii) Presence of coarse constituents from ingot casting [14].

(iii) Segregation of tramp elements such as sodium, potassium and sulphur to grain boundaries [7].

(iv) Dislocations shearing the coherent and partially coherent matrix strengthening precipitates. This results in localization of slip along preferential crystallographic planes [15-18]. Strain localization in the coarse planar slip bands occurs due to heterogeneity of slip. The localization of strain in slip bands results in build-up of high stresses at the grain boundaries. The high stress concentrations at the grain and sub-grain boundaries causes them to open up resulting in low energy intergranular rupture. This process is responsible for lowering the ductility and toughness of the material with increased ageing to peak strength [19].

(v) Planar slip deformation is exacerbated by the presence of precipitate-free zones which enhances the stress concentrations at: (a) grain boundaries, and (b) grain boundary triple junctions [20-22].

Various modifications in alloy chemistry and processing techniques have been used in an attempt to improve the ductility as also the fracture toughness of these alloys while maintaining the benefit of high strength. Ternary solute additions to the aluminium-lithium system such as magnesium, copper and

\*Presently Program Director, Materials Engineering and Processing, National Science Foundation, Washington D.C., USA.

zirconium have been found to have beneficial effects [23]. Magnesium and copper improve the strength of the alloy by coprecipitating with  $\delta'$  ( $\text{Al}_3\text{Li}$ ) and/or incorporating lithium to form coherent and partially coherent ternary phases. Coprecipitation is effective because it increases the strength of the alloy and promotes homogeneous deformation. Besides, magnesium reduces the solubility of lithium in the matrix during the early stages of ageing and increases the volume fraction of the coherent, ordered strengthening precipitate,  $\delta'$  ( $\text{Al}_3\text{Li}$ ) [24]. Magnesium also provides an increment of solid solution strengthening and eliminates the formation of precipitate-free zones (PFZs) near grain boundaries by precipitating as  $S''$  or  $S'$  ( $\text{Al}_2\text{CuMg}$ ).

This paper describes the relationship between microstructure, tensile properties and fracture characteristics of the quaternary lithium-containing aluminium alloy 8090. The kinetics of the fracture process are discussed in the light of competing mechanistic effects involving: (i) intrinsic microstructural features, (ii) deformation behaviour, and (iii) micromechanisms which promote failure.

## 2. Material and experimental procedures

The Al–Li–Cu–Mg alloy 8090 used in this study was obtained from the US Navy, Naval Surface Weapons Center. The alloy was provided in the form of an extruded plate of cross-section 100 mm  $\times$  25 mm (4 in  $\times$  1 in) in the T851 condition. The chemical composition (in weight percent) of the alloy is given in Table I.

The iron and silicon elements in the alloy are impurities. During ingot solidification and subsequent processing, these impurities precipitate as insoluble constituent phases,  $\text{Al}_3\text{Fe}$  and  $\text{Al}_7\text{Cu}_2\text{Fe}$ . Zirconium additions result in the formation of metastable cubic  $\text{Al}_3\text{Zr}$  precipitates which are spherical in morphology and can effectively pin the grain and subgrain boundaries. The cubic  $\text{Al}_3\text{Zr}$  ( $\beta'$ ) phase also known as dispersoids has an  $\text{Ll}_2$  crystal structure and nucleates heterogeneously on dislocations and grain boundaries [25, 26]. The dispersoid particle ( $\text{Al}_3\text{Zr}$ ) is coherent with the matrix and aids in (i) retarding subgrain boundary migration and coalescence, (ii) suppressing recrystallization, (iii) controlling grain growth, and (iv) stabilizing the subgrain structure [27]. The major strengthening precipitates in the ternary Al–Cu–Li alloys are  $\delta'$  ( $\text{Al}_3\text{Li}$ ),  $T_1$  ( $\text{Al}_2\text{CuLi}$ )  $\theta''$  ( $\text{Al}_2\text{Cu}$ ) and  $\theta'$  ( $\text{Al}_2\text{Cu}$ ) [28–32] where  $\theta''$  and  $\theta'$  are analogous to the intermediate precipitates found in binary aluminium–copper alloys. In the peak-aged, maximum strength condition the Al–Li–Cu alloys contain precipitate free zones along the grain and subgrain boundaries [21, 32]. Magnesium additions to a ternary Al–Li–Cu alloy provides solid solution strengthening and eliminates

the formation of precipitate free zones through the precipitation of  $S''$  and  $S'$  ( $\text{Al}_2\text{CuMg}$ ) phases near the grain boundaries [24]. The T851 heat treatment on the extruded plate is summarized in detail elsewhere and will not be repeated here [34].

Metallographic samples were cut from the three orthogonal directions of the extruded plate, mounted in bakelite and wet-ground on 320, 400 and 600 grit silicon carbide (SiC) paper using water as a lubricant and then mechanically polished with 1 and 0.05  $\mu\text{m}$  alumina-based lubricants. Grain morphology was revealed using a Keller's etch. Size and distribution of the soluble phases was determined using a hot (50°C) 10% orthophosphoric acid solution as the etchant. The specimens were etched for 180 sec, and examined by optical electron microscopy and photographed using a standard bright field technique. A hot bromine etch procedure was used to analyse the size, morphology and distribution of the insoluble and high temperature precipitating phases. The bromine-etch procedure involved submersing samples in a boiling solution mixture of 10% bromine in methanol for 60 sec. The solution selectively attacks the aluminium matrix and exposes the coarse constituent phases. The etched specimens were examined by scanning electron microscopy.

Tensile tests were performed on specimens ASTM standard smooth, cylindrical specimens of 35 mm gauge length and 6.35 mm diameter. The stress axes of the cylindrical samples were parallel (longitudinal) or perpendicular (transverse) to the extrusion direction. Tests were performed on a closed-loop servo-hydraulic testing machine with an initial strain rate of  $6 \times 10^{-4} \text{sec}^{-1}$ . The load–displacement curves were obtained on a strip-chart recorder. The diameter of the tensile samples were measured using a micrometer, before and after testing.

Fracture surfaces of the tensile samples were examined in a scanning electron microscope (SEM) so as to determine the predominant fracture mode and to characterize the fine scale fracture features on the surface.

## 3. Results and discussion

### 3.1. Microstructures

The microstructures of the as-received Al–2.8Li–1.3Cu–0.7Mg–0.12Zr alloy 8090 is shown in Fig. 1 as a triplanar optical micrograph illustrating the grain structure of the material in the three orthogonal directions of the extruded plate. This material is partially recrystallized with the unrecrystallized grains flattened and elongated in the longitudinal direction, as a consequence of deformation introduced during extrusion. The transverse grains appeared to have a large aspect ratio (Fig. 1). The grain and subgrain boundaries were observed to be decorated with a fine dispersion of second-phase particles that are: (a) the

TABLE I Composition (weight per cent) of aluminium alloy 8090

Element	Li	Cu	Mg	Zr*	Fe	Si	Zn	Ti	Al
Amount (wt %)	2.8	1.3	0.7	0.12	0.05	0.02	0.03	0.03	Bal.

\*Grain refiner, present as  $\text{Al}_3\text{Zr}$ .

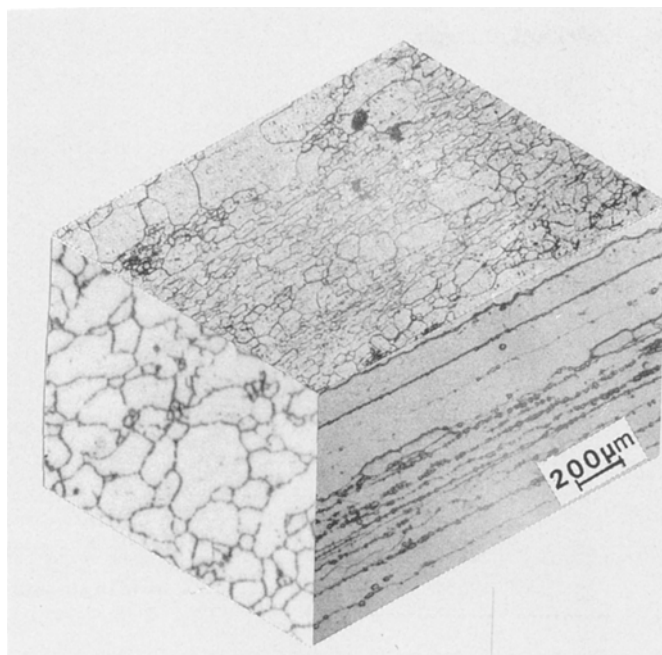


Figure 1 Triplanar optical micrograph illustrating the grain size and morphology of aluminium alloy 8090 extruded plate.

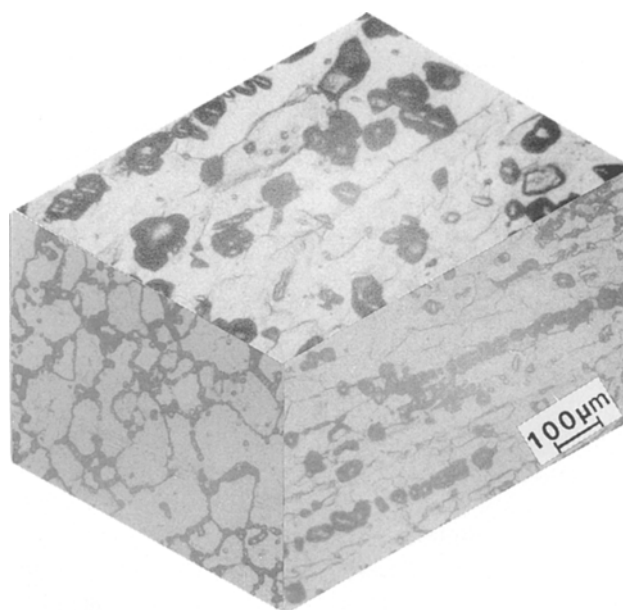


Figure 2 Triplanar optical micrograph illustrating particle density and distribution along the three orthogonal directions of the extruded plate.

equilibrium phases [ $\delta(\text{AlLi})$ ,  $\text{S}(\text{Al}_2\text{CuMg})$  and T-type ( $\text{Al}_x\text{Cu}_y\text{Li}_z$ )], (b) the coarse iron-rich intermetallics, and (c) the magnesium-rich insoluble phases (Fig. 2). In an earlier study by Crooks and Starke [24] on an  $\text{Al-3Cu-1.58Li-0.79Mg-0.20Zr}$  alloy, these particles were identified as

(i) the lithium-rich equilibrium phase,  $\text{T}_2(\text{Al}_6\text{-CuLi}_3)$  that occurs in the form of massive round particles, and

(ii) the equilibrium  $\text{S}(\text{Al}_2\text{CuMg})$  phase.

At higher magnification, the insoluble and partially soluble constituent particles were observed to be stratified and distributed along the extrusion direction of the plate (Fig. 2). At regular intervals along the longitudinal (extrusion) direction of the as-received plate, clustering of the constituent particles was observed (Fig. 3). The distribution of larger insoluble constituent particles was revealed by bromine etching. The density of these particles is greater in the longi-

tudinal direction than in the transverse direction of the extruded plate [34]. Fig. 4 reveals the morphology of an iron-rich intermetallic particle identified as  $\text{Al}_7\text{Cu}_2\text{Fe}$  by selected area diffraction [35].

### 3.2. Tensile properties

A compilation of the monotonic mechanical properties of the 8090 alloy, in the longitudinal (L) and transverse (T) directions is given in Table II. Multiple (three) samples were tested for each condition and no significant variation between the samples was observed.

The yield strength ( $\sigma_{0.2}$ ) in the transverse (T) direction (443 MPa) is 23% lower than the corresponding value in the longitudinal (L) direction (578 MPa). The tensile strength ( $\sigma_{\text{UTS}}$ ) in the transverse direction (536 MPa) is 11% lower than in the longitudinal direction (600 MPa). The elongation to failure (ductility) in the transverse (T) direction (8.40%) shows over a 100% improvement than the corresponding value in

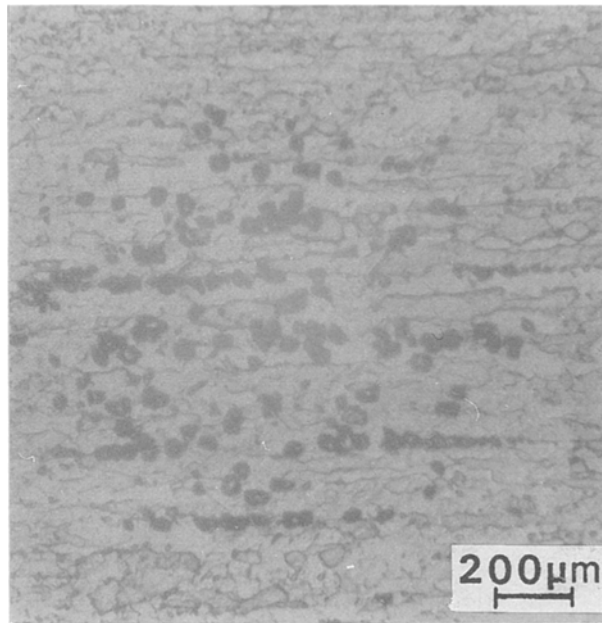


Figure 3 Optical micrograph showing "clustering" of the intermetallic particles in the extrusion direction of the 8090-T851 plate.

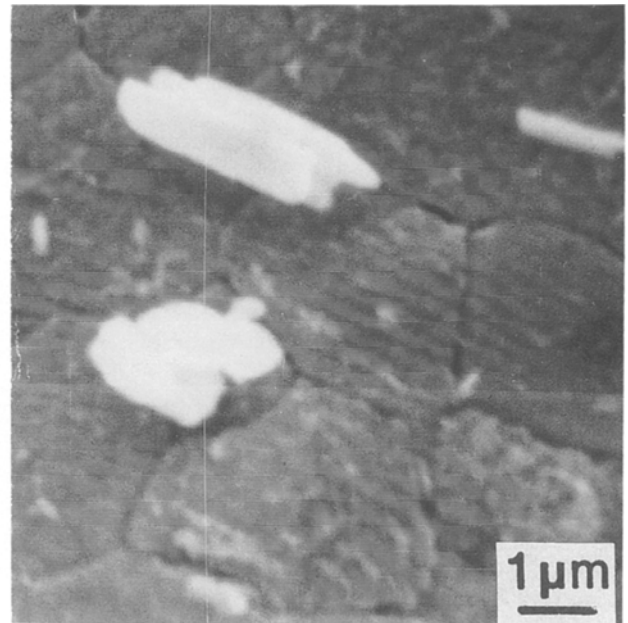


Figure 4 Scanning electron micrograph showing morphology of an iron-rich metallic ( $Al_7Cu_2Fe$ ) on bromine-etched surface of alloy 8090 (T851 condition).

the longitudinal (L) direction (3.90%) of the extruded plate. The percentage reduction in area (RA) in the transverse direction (7.40%) also shows a 170% improvement over the corresponding value in the longitudinal direction (2.70%). The true fracture stress ( $\sigma_f$ ) in the longitudinal direction (617 MPa) is marginally higher (8%) than the corresponding value in the transverse direction (574 MPa).

The elastic modulus ( $E$ ) obtained by the extensometer trace, accords well in the two directions (longitudinal and transverse). Barring the low ductility in the longitudinal (extrusion) direction, the alloy in the T851 temper has property combinations which are attractive for aerospace applications. A comparison of the monotonic properties of aluminium alloy 8090 with other candidate aluminium alloys (orientation: longitudinal) is made in Table III. The variation of yield strength (MPa) with total elongation (percent) for a limited selection of aluminium alloys is shown in Fig. 5.

### 3.3. Deformation and fracture characteristics

The monotonic fracture surfaces are helpful in elucidating microstructural effects on the ductility and fracture properties of alloy 8090. Extensive fractography of the tensile samples revealed

- (i) transgranular shear failure,
- (ii) cracking along the grain boundaries or intergranular failure,

- (iii) intersubgranular failure along the subgrain boundaries, and

- (iv) void formation at the grain and subgrain boundaries.

Representative fracture features of the samples are shown for both the longitudinal and transverse orientations.

On a macroscopic scale, tensile fracture of alloy 8090-T851 in the longitudinal direction was predominantly shear. The fracture surface was oriented approximately  $45^\circ$  to the major stress axis, following the plane of maximum shear stress (Fig. 6a). The shear-type of fracture tends to minimize necking and thus the triaxial state of stress and hydrostatic component that occurs in a necked region [36]. Consequently, void nucleation at the coarse constituent and intermediate size dispersoid particles is affected.

Long secondary cracks, or ledges were observed on the fracture surfaces, separating the transgranular and intergranular regions, with the crack plane oriented parallel to the loading axis which also was the extrusion direction (Fig. 6b). The tendency toward localized inhomogeneous planar deformation due to the interaction of mobile dislocations with the ordered coherent and partially coherent precipitate particles dispersed in the matrix of lithium-containing aluminium alloys results in strain localization. For the alloy (Al-Li-Cu-Mg) and in the ageing condition

TABLE II Monotonic mechanical properties of aluminum alloy 8090

Orientation	Modulus of elasticity (GPa)	0.2% Proof stress (MPa)	UTS (MPa)	Elongation (%)	Reduction in area (%)	True fracture stress (MPa)
Longitudinal	82.8	578	600	3.9	2.7	617
Long transverse	82.8	443	536	8.4	7.4	574

Average of three tests. Gauge length 35 mm, diameter 6.35 mm. Room temperature.

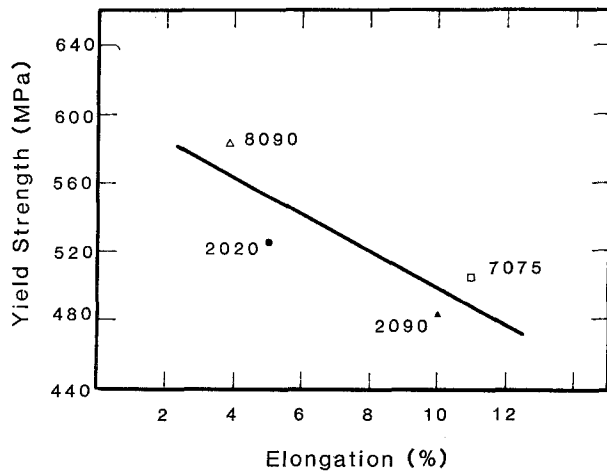


Figure 5 Comparison of yield strength against elongation of alloy 8090 with a limited selection of commercial aluminium alloys.

(peak-aged) studied, the coarse planar slip bands resulting from the interaction of dislocations with the precipitate particles, impinge upon grain boundaries and causes strain concentration or localization at their point of impingement on the grain boundary. The magnitude of strain concentration in the vicinity of grain boundaries depends on the slip length. The high concentration of strain due to localized planar deformation causes a large stress build-up at the grain boundary. Stress concentration accelerates the fracture process through the initiation of microcracks at the grain boundary resulting in ledge type intergranular fracture (Fig. 7), and voids at the coarse constituent particles and equilibrium precipitates along the grain boundary.

The intermetallics in this alloy are the iron-rich particles and the magnesium-rich insoluble phases. During plastic deformation, nucleation of cracks occurs by: (i) the cracking of coarse constituent particles [37], (ii) through particle-matrix interface separation [38, 39], and (iii) at areas of poor interparticle bonding [40, 41]. Interfacial strength is a

dominant factor in crack nucleation. There are several other factors which though secondary and indirect compared to particle-matrix separation contribute to the void initiation process. These include: size of the second-phase particle, particle shape and volume fraction, particle strength, particle location and distribution [42]. Void initiation at the second-phase particles is a complex combination of inclusion size, stress and local strain levels, and local deformation modes which cannot be generalized. The presence of fairly large-sized second-phase particles in alloy 8090 facilitates the nucleation of cracks at low stresses. Void nucleation at a second-phase particle occurs when the elastic energy in the particle exceeds the surface energy of the newly formed void surfaces [37]. For the case of spherical particles, the critical stress for particle cracking is

$$\sigma = (6\gamma E/q^2 d)^{0.5} \quad (1)$$

where  $\gamma$  is the surface energy of the particle,  $q$  the stress concentration factor at the particle,  $E$  the Young's Modulus of the particle, and  $d$  the particle diameter.

While satisfaction of Equation 1 is a necessary condition for void initiation, it must also be aided by a stress on the particle-matrix interface in excess of the interfacial strength [43]. When the stress at the particle-matrix interface reaches a critical value, void nucleation occurs by interface separation. The interface stress ( $\sigma_1$ ) at a particle comprises of the applied stress,  $\sigma_A$ , and the normal stress due to blocked slip bands,  $\sigma_p$

$$\sigma_1 = \sigma_A + \sigma_p = \sigma_A + kF(r)^{0.5} \quad (2)$$

In Equation 2,  $\sigma_p$  is equated to the product of the constant,  $k$ , the flow stress  $F$ , and the square root of the slip band length,  $r$  [44].

When a critical value of  $\sigma_1$  is reached, void nucleation occurs provided sufficient elastic energy is available to create new void surfaces. Furthermore, in systems containing a large volume fraction of second-

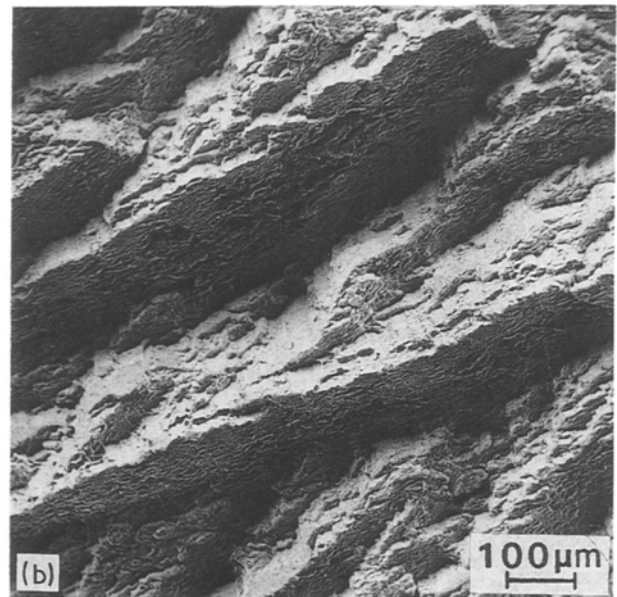
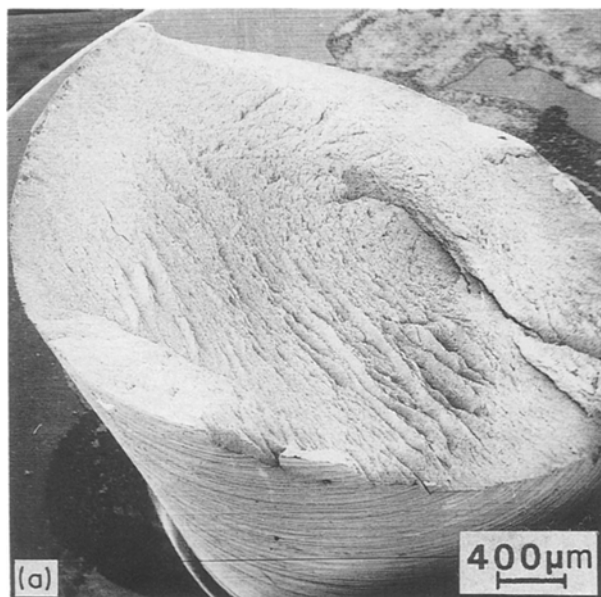


Figure 6 Scanning electron micrograph of fracture surface of longitudinal tensile sample showing (a) shear-type fracture, and (b) high magnification showing large secondary cracks or ledges parallel to the extrusion direction.

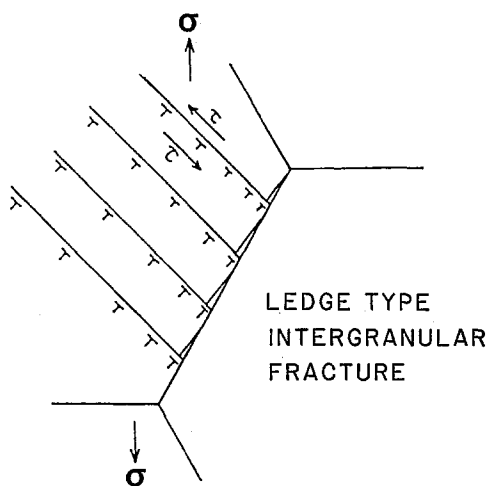


Figure 7 Schematic representation of ledge-type intergranular fracture.

phase particles there exists an intrinsic particle-size effect on void nucleation [45]. The influence of particle size is caused by the interaction of stress fields of closely spaced inclusions.

Coalescence of the microvoids is a distinct phase or the last stage in the fracture process. During coalescence void-void interactions occur during which period void growth is accelerated. In this alloy void coalescence results from the formation of void sheets at the small second-phase particles (such as the  $\text{Al}_3\text{Zr}$  dispersoids) in conjunction with void impingement, that is, voids growing until they touch. Since the number of microconstituents (inclusions and constituent particles) is large, some of the large voids which are created by fracture of the iron-rich intermetallic particles coalesce by impingement. The more widely separated voids coalesce by the formation of void sheets. Coalescence of microvoids initiated at grain boundary precipitates results in dimple-formation type intergranular fracture (Fig. 8). The transgranular fracture regions comprised of pronounced cracking along the subgrain boundaries, parallel to the major stress axis (Fig. 9). The transgranular regions were lacking in features (Fig. 10).

The subgrain structures in the unrecrystallized regions have a marked influence on the fracture characteristics of the quaternary alloy. The subgrains in the maximum strength, peak-aged condition, are well developed. Due to a low degree of misorientation between neighbouring subgrains, the impact of grain boundaries as barriers to the dislocation motion is reduced. This tends to increase the "effective" slip

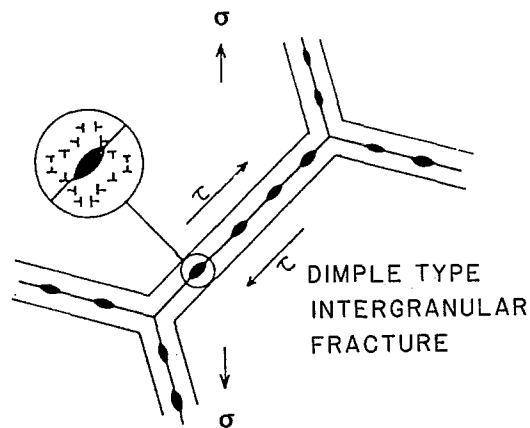


Figure 8 Schematic representation of the dimple-formation type intergranular fracture.

length with concomitant reduction in ductility. The poor ductility of alloy 8090 in the peak-aged condition is not a consequence of planar deformation *per se*, but also of its occurrence with a strong crystallographic texture. Micro-dimples were observed on the intersubgranular fracture surface (Fig. 11). The dimples are the result of the presence of smaller second phase particles, that is, the zirconium dispersoids ( $\text{Al}_3\text{Zr}$ ), and the T-type ( $\text{Al}_x\text{Cu}_y\text{Li}_z$ ) precipitates. The equilibrium  $\delta$  ( $\text{AlLi}$ ) and  $\text{Al}_2\text{MgLi}$  phases along the grain and subgrain boundaries promote intergranular void coalescence.

The micromechanisms governing the deformation and fracture characteristics of an age hardenable aluminium alloy depend on the intrinsic microstructural features such as: (i) coherency and distribution of the matrix precipitates, (ii) grain size and shape, (iii) grain boundary precipitates, and (iv) presence of other second-phase particles including the dispersoids and insoluble constituent particles which result from the presence of iron and silicon impurities. Consideration of the strengthening mechanism in the peak-aged alloy is important because it markedly affects the deformation process. During deformation, the ordered coherent and partially coherent precipitate particles [ $\delta'$  ( $\text{Al}_3\text{Li}$ ),  $\text{T}_1$  ( $\text{Al}_2\text{CuLi}$ )  $\theta'$  ( $\text{Al}_2\text{Cu}$ ) and  $\text{S}'$  ( $\text{Al}_2\text{CuMg}$ )] in the alloy are easily sheared by the motion of dislocations on close-packed  $\{111\}$  planes and in the close-packed directions. The motion of unit dislocations through an ordered lattice of the precipitate results in disorder in the form of an antiphase boundary (APB). Once the precipitate particles are disordered and slip has occurred on one plane, the area

TABLE III Comparison of the monotonic mechanical properties of alloy 8090 with other aluminium alloys

Alloy	Temper	Elastic modulus (GPa)	Yield strength (MPa)	Ultimate strength (MPa)	Elongation (%)
Aluminium* (96%)	-	-	30	70	43.0
2020	T651	77	526	567	5.0
2090	T851	79	485	533	10.0
8090	T851	83	578	600	3.85
2024	T851	72	450	485	6.0
7075	T651	71	505	570	11.0

\*from Aluminum by J. E. Hatch.

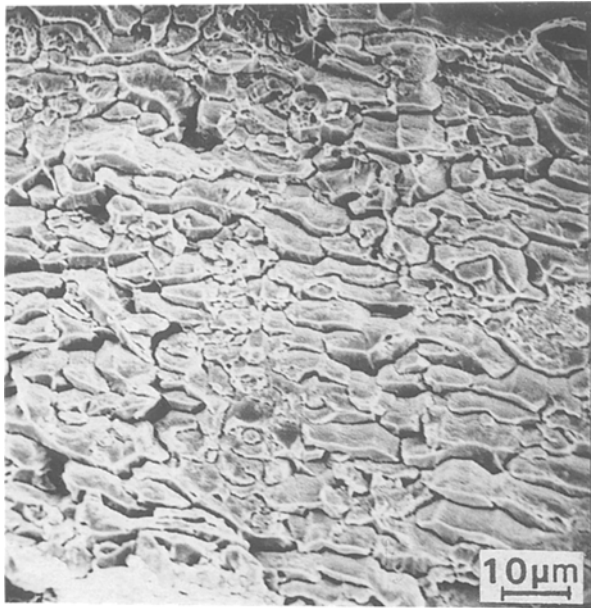


Figure 9 Scanning electron micrograph of the longitudinal tensile sample showing the transgranular region with fracture along the subgrain boundaries.

of the APB is decreased, thus favouring additional deformation on that plane [20, 46]. The concentration of deformation in planar slip bands leads to strain localization at their point of impingement on the grain boundary. The localized planar deformation produces large stress concentrations at the grain boundary. The increased strength of the age-hardened matrix in the peak-aged condition renders nucleation of flow across the boundary difficult. This effect coupled with the presence of grain boundary precipitates results in enhanced deformation along the grain boundaries and concomitant low ductility; as compared to conventional aluminium alloys of comparable strength. Void initiation results at the intersection of a slip band and a coarse grain boundary precipitate (Fig. 8). The applied stress assists in the growth of voids. Linking of

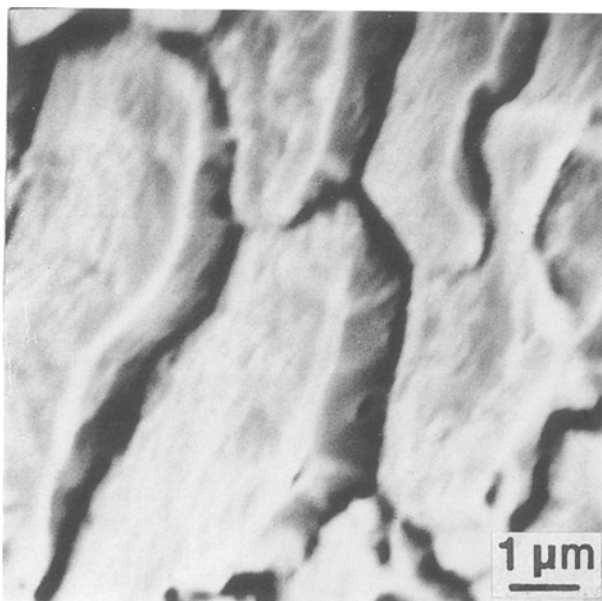


Figure 10 High magnification fractograph of the longitudinal tensile sample of alloy 8090 showing fine intergranular cracking along the subgrain boundaries and featureless transgranular region.

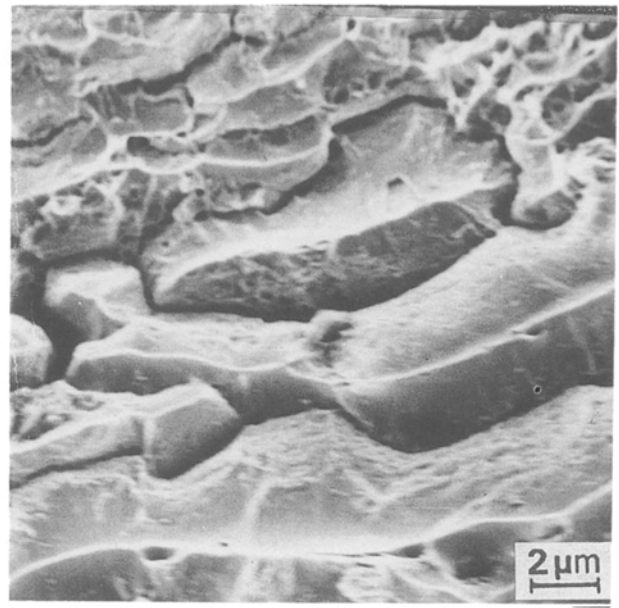


Figure 11 Scanning electron micrograph showing ductile dimples covering the intergranular fracture regions.

similar voids is an additional factor that promotes and/or enhances intergranular fracture.

On a macroscopic scale, fracture of the transverse sample was essentially normal to the stress axis (Fig. 12a). Laminar cracks were observed separating the transgranular and intergranular regions and extending down the fracture surface parallel to the loading direction (Fig. 12b). The spacing between the laminar cracks is associated with fracture along the grain boundaries. The tendency for intergranular failure and the sequence of events that result in necking and failure of the grains has been discussed by Srivatsan and Coyne [41] and Starke and Lin [14] for a ternary Al-Cu-Li alloy. The lateral separation of grains, which occurs under the action of triaxial stresses in plane strain, minimizes the constraints imposed by the neighbouring grains during plastic deformation. The lateral separation results in

- (i) macroscopic cracking along the recrystallized and unrecrystallized grain boundaries (Fig. 13a), and
- (ii) microscopic cracking along the individual subgrains (Fig. 14a).

The fracture path along the grain and subgrain boundaries is shown diagrammatically in Figs 13b and 14b. The transgranular fracture regions were covered with a network of very fine dimples. These fine dimples are associated with the iron- and silicon-rich constituents, the zirconium dispersoids, and the equilibrium  $\delta(\text{AlLi})$  and T-type ( $\text{Al}_x\text{Cu}_y\text{Li}_z$ ) precipitates.

#### 4. Summary and concluding remarks

The general conclusions of the present study of the microstructure, tensile properties and fracture characteristics of an Al-Cu-Li-Mg-Zr alloy is summarized as follows.

- (1) The alloy was partially recrystallized with the grains elongated parallel to the extrusion direction. The unrecrystallized grains comprised of well developed subgrains. The grain and subgrain boundaries were decorated with particles.

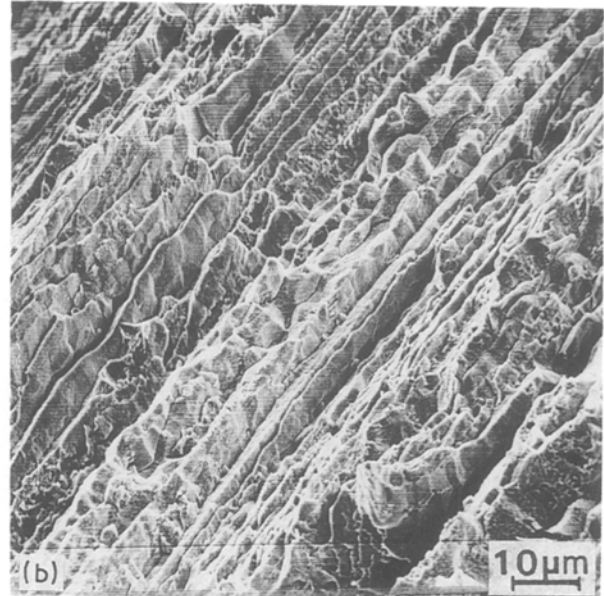
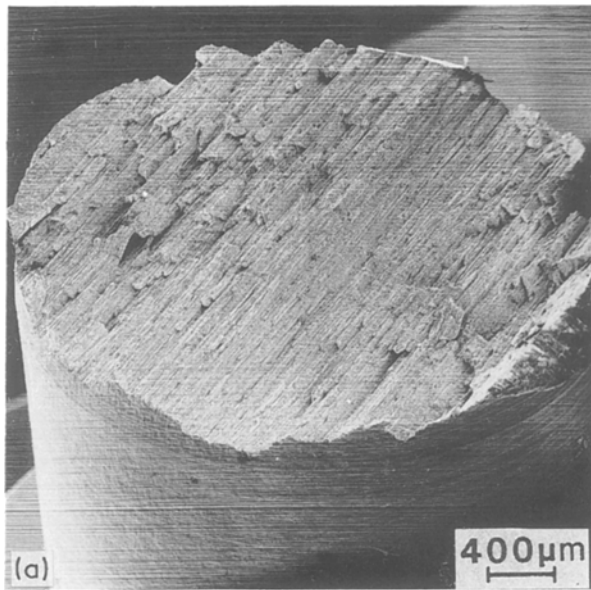


Figure 12 Scanning electron micrograph of the fracture surfaces of the transverse tensile sample showing: (a) fracture normal to the stress axis, and (b) laminar cracks parallel to the major stress axis, T851 condition.

(2) The double ageing treatment (32 h at 65° C plus 40 h at 52° C) resulted in an alloy having high strength ( $\sigma_{0.2}$  yield strength = 578 MPa and ultimate tensile strength = 600 MPa) with total elongation of 3.90% and reduction in area of 2.70% in the longitudinal (extrusion) direction. The total elongation (8.40%) to failure and reduction in area (7.40%) was higher (200 to 300%) in the transverse direction of the extruded plate than in longitudinal direction.

(3) Fracture in the maximum strength, peak-aged condition was low energy intergranular and intersub-granular separation, with fracture associated with the grain and subgrain boundaries.

Results of this study provide information on the

role of grain structure, second-phase particles and matrix strengthening precipitates on the fracture behaviour of the high strength Al-1.3Cu-2.8Li-0.7Mg-0.12Zr alloy. The overall fracture process is governed by a complex interplay between the presence of coarse microconstituents, the matrix deformation characteristics and grain boundary failure.

#### Acknowledgements

This work was supported by the US Navy, Naval Surface Weapons Center under contract No. N60921-86-M-7570, Program Manager Mr A. P. Divecha. The authors thank Mrs Sandra Collins for her timely assistance in the preparation of this manuscript.

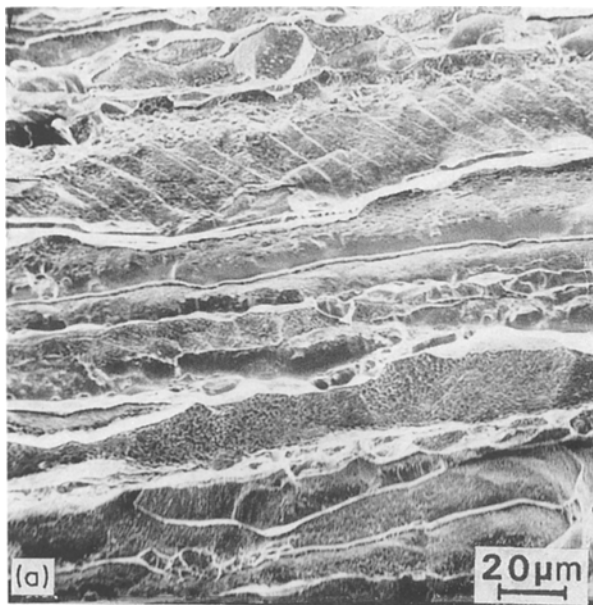


Figure 13 (a) Scanning electron micrograph of transverse tensile sample showing intergranular cracking along the large unrecrystallized grain boundaries with fine ductile dimples on the transgranular fracture surface. (b) Schematic showing failure mode along the large unrecrystallized grain boundaries of alloy 8090.

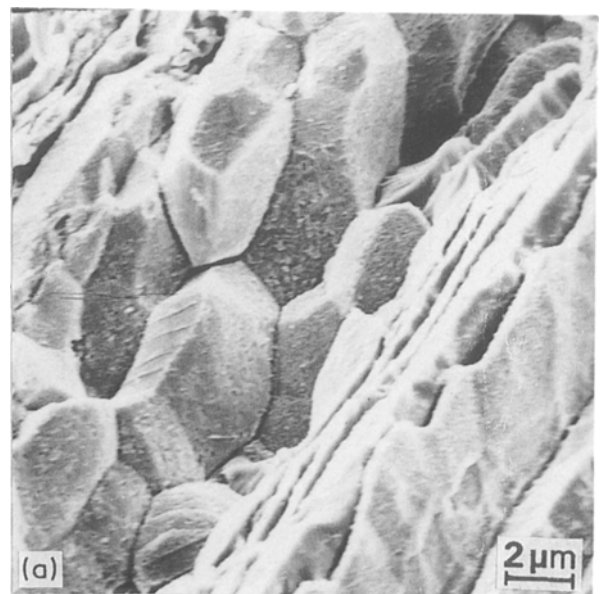


Figure 14 (a) High magnification fractograph of ridge showing intergranular cracking along the subgrain boundaries. (b) Schematic showing intergranular cracking along the subgrains within an unrecrystallized grain.

## References

1. E. A. STARKE, Jr. and T. H. SANDERS, Jr., (eds) Aluminum-Lithium Alloys, Proceedings of the First International Conference on Aluminum-Lithium Alloys, AIME, Warrendale, PA, 1981.
2. E. A. STARKE, Jr. and T. H. SANDERS, Jr., (eds) Aluminum-Lithium Alloys II, Proceedings of the Second International Conference on Aluminum-Lithium Alloys, Monterey, AIME, Warrendale, PA, 1984 (Metallurgical Society of AIME, Warrendale, PA, 1985).
3. C. BAKER, P. J. GREGSON, S. J. HARRIS and C. J. PEEL, (eds), Aluminum-Lithium Alloys III, Proceedings of the Third International Conference on Aluminum-Lithium Alloys (Institute of Metals, London, UK, 1986).
4. E. A. STARKE, Jr. and T. H. SANDERS, Jr., (eds) Aluminum Alloys: Their Physical and Mechanical Properties, Proceedings of the First International Conference on Aluminum Alloys, EMAS, England, 1986 (Engineering Materials Advisory Services, England, 1986).
5. Aluminum-Lithium Alloys IV, Proceedings of the Fourth International Conference on Aluminum-Lithium Alloys, Paris, France, 1987 (in press).
6. A. K. VASUDEVAN, A. C. MILLER and M. M. KER-SKER, in Aluminum-Lithium Alloys II, Proceedings of the Second International Conference on Aluminum-Lithium Alloys, edited by T. H. Sanders, Jr. and E. A. Starke, Jr. (AIME, Warrendale, PA, 1984) p. 81.
7. A. K. VASUDEVAN, E. A. LUDWICZAK and S. F. BAUMANN, *Mater. Sci. Eng.* **72** (1985) L-25.
8. P. N. T. UNWIN and G. C. SMITH, *J. Inst. Met.* **97** (1969) 299.
9. A. J. CORNISH and M. K. B. DAY, *ibid.* **99** (1971) 377.
10. T. KAWABATA and O. IZUMI, *J. Mater. Sci.* **11** (1976) 892.
11. *Idem.*, *ibid.* **14** (1979) 1071.
12. A. K. VASUDEVAN, E. A. LUDWICZAK, S. F. BAUMANN, P. R. HOWELL, R. D. DOHERTY and M. M. KER-SKER, *Mater. Sci. Technol.* **2** (1986) 1205.
13. M. GRAF and E. HORNBOGEN, *Acta Metall.* **25** (1977) 883.
14. E. A. STARKE, Jr. and F. S. LIN, *Metall. Trans.* **13A** (1982) 2259.
15. T. H. SANDERS, Jr. and E. A. STARKE, Jr., *Acta Metall.* **32** (1982) 927.
16. P. J. GREGSON and H. M. FLOWER, *ibid.* **33** (1985) 527.
17. B. NOBLE, S. J. HARRIS and K. DINSDALE, *Met. Sci.* **16** (1982) 425.
18. A. K. VASUDEVAN and S. SURESH, *Mater. Sci. Eng.* **72** (1985) 37.
19. S. SURESH, A. K. VASUDEVAN, M. H. TOSTEN and P. R. HOWELL, *Acta Metall.* **35** (1987) 25.
20. T. H. SANDERS, Jr., E. A. LUDWICZAK and R. R. SAWTELL, *Mater. Sci. Eng.* **43** (1980) 247.
21. F. S. LIN, S. B. CHAKRABORTTY and E. A. STARKE, Jr., *Metall. Trans.* **13A** (1982) 401.
22. E. A. STARKE, Jr., in "Strength of Metals and Alloys, Proceedings of the International Conference on Strength of Metals and Alloys", edited by R. C. Gifkins (Pergamon, Oxford, 1983) p. 1025.
23. E. A. STARKE, Jr., T. H. SANDERS, Jr. and I. G. PALMER, *J. Met.* **3** (1980) 24.
24. R. E. CROOKS and E. A. STARKE, Jr., *Metall. Trans.* **15A** (1984) 1367.
25. E. NESS and N. RYUM, *Scripta Metall.* **5** (1971) 987.
26. R. J. RIOJA and E. A. LUDWICZAK, in Aluminum-Lithium Alloys III, Proceedings of the Third International Conference on Aluminum-Lithium Alloys, edited by C. Baker, S. J. Harris, B. Noble and C. J. Peel (Institute of Metals, London, 1985).
27. J. M. GALBRAITH, M. H. TOSTEN and P. R. HOWELL, *J. Mater. Sci.* **22** (1987) 27.
28. J. M. SILCOCK, *J. Inst. Met.* **88** (1959-60) 357.
29. B. NOBLE and G. E. THOMPSON, *Met. Sci. J.* **6** (1972) 167.
30. K. SCHNEIDER and M. von HEIMENDHAL, *Z. Metallkde.* **64** (1973) 342.
31. J. G. RINKER, M. MAREK and T. H. SANDERS, Jr., *Mater. Sci. Eng.* **64** (1984) 203.
32. T. S. SRIVATSAN, E. J. COYNE, Jr. and E. A. STARKE, Jr., *J. Mater. Sci.* **21** (1986) 1553.
33. M. H. TOSTEN, A. K. VASUDEVAN, and P. R. HOWELL, *Metall. Trans.* **19A** (1988) 51.
34. T. S. SRIVATSAN, Final Report to US Navy, Naval Surface Weapons Center, Contract No. N60921-M-7570, June 1987.
35. A. MUNITZ, A. ZANGVIL and M. METZGER, *Metall. Trans.* **11A** (1980) 1863.
36. W. X. FENG, F. S. LIN and E. A. STARKE, Jr., *Metall. Trans.* **15A** (1984) 1209.
37. J. GURLAND and J. PLATEAU, *Transactions ASM*, **56** (1963) 442.
38. R. H. VAN STONE and J. A. PSIODA, *Metall. Trans.* **6A** (1975) 672.
39. R. H. VAN STONE, J. R. LOW and J. L. SHANNON, Jr., *ibid.* **9A** (1978) 539.
40. R. H. VAN STONE, T. B. COX, J. R. LOW, Jr. and J. A. PSIODA, *Int. Met. Rev.* **30** (1985) 157.
41. T. S. SRIVATSAN and E. J. COYNE, Jr., *Mater. Sci. Technol.* **3** (1987) 130.
42. A. W. THOMPSON, *Metall. Trans.* **18A** (1987) 1877.
43. A. S. ARGON, J. IM and A. NEEDLEMAN, *ibid.* **6A** (1975) 825.
44. C. ZENER, "Elasticity and Anelasticity", (University of Chicago Press, Chicago, 1948) p. 130.
45. A. S. ARGON, *J. Eng. Mater. Technol.* **98** (1976) 60.
46. R. F. DECKER, *Metall. Trans.* **4A** (1973) 2495.

Received 15 March  
and accepted 28 July 1988